

Continuous magnetohydrodynamic spectra of two-dimensional coronal magnetostatic flux tubes

A.J.C. Beliën, S. Poedts, and J.P. Goedbloed

FOM-Institute for Plasma Physics 'Rijnhuizen', P.O.Box 1207, 3430 BE Nieuwegein, The Netherlands

Received 25 September 1996 / Accepted 12 December 1996

Abstract. In this paper we derive the equations for the continuous ideal magnetohydrodynamic (MHD) spectrum of two-dimensional coronal loops, including gravity and expansion, in general curvilinear coordinates. The equations clearly show the coupling between Alfvén and slow magnetosonic continuum waves when both pressure and geodesic curvature of the magnetic field lines are present. Gravity always gives rise to Alfvén-slow mode coupling when the magnetic field is twisted. Numerical calculations show that the coupling of Alfvén and slow magnetosonic continuum waves can be strong, especially for Alfvén-like continuum waves, when the magnetic flux concentration near the bases of flux tubes is taken into account. Amplitude ratios of the parallel and perpendicular displacement components of 0.4 were obtained for concentration of the flux with a factor of 4. Gravity has less effect on the coupling of Alfvén and slow magnetosonic continuum waves than the concentration of flux but it has a large influence on the low frequency slow magnetosonic-like continuum branches.

Key words: MHD – Sun: corona – waves

1. Introduction

The recently observed standing waves in the chromospheric and low transition regions of the sun by Bocchialini & Baudin (1995) provide new support for wave heating theories of the solar corona. Like all proposed heating mechanisms of the solar corona, see the review by Zirker (1993), magnetic wave heating depends on the creation of small length scales to obtain effective magnetic diffusion times. In wave heating of closed loop systems, the creation of these small length scales is tightly connected to another important phenomenon: resonances. These resonances occur due to the large density gradients in the low chromosphere and photosphere, which effectively turn coronal loops into resonant cavities (Hollweg 1984). The resonances yield standing waves which are

dissipated by non-ideal mechanisms and, hence, heat the plasma. The conversion of magnetic energy into heat is efficient for waves with frequencies that lie within certain intervals, the so-called continuum frequency ranges. Resonant absorption was first introduced as a possible heating mechanism for the solar corona by Ionson (1978). Since then many papers on the subject have appeared; see, e.g., Kuperus et al. (1981), Heyvaerts & Priest (1983), Davila (1987), Grossmann & Smith (1988), Poedts et al. (1989), Poedts & Kerner (1992), Halberstadt & Goedbloed (1995a, 1995b), Ofman et al. (1995), Poedts & Boynton (1996), Ofman & Davila (1996).

In linearized ideal magnetohydrodynamics (MHD) two types of continua exist which are commonly referred to as Alfvén and slow magnetosonic although this classification is, strictly speaking, only valid for one-dimensional equilibrium configurations. Because each magnetic surface has its own characteristic set of discrete frequencies, due to the assumed inhomogeneity of the equilibrium, corresponding sets of continua are traced out when one scans over these surfaces. The continuum eigenoscillations are singular at the resonant surfaces. It is really this singular behavior that is responsible for the heating mechanisms based on resonant absorption of Alfvén waves. When non-ideal effects are taken into account, continua no longer exist and they are replaced by closely spaced damped discrete eigenmodes with frequencies located in the ideal continuum ranges. These modes still possess very large gradients which are responsible for short magnetic diffusion times and, hence, for efficient heating. Continua and the associated singular behavior of magnetic field lines and surfaces have been the subject of a lot of research (see, e.g., Tataronis & Grossmann 1973, Chen & Hasegawa 1974, Goedbloed 1975, Krylov et al. 1979, Hameiri 1981, Krylov & Lifschitz 1984, Southwood & Kivelson 1986, Mond et al. 1990, Poedts & Goossens 1991, Halberstadt & Goedbloed 1993, Goedbloed & Halberstadt 1994) and the results have found applications not only in coronal but also in nuclear fusion and magnetospheric contexts.

In most studies of MHD wave activity and heating, the effects of the huge difference in the physical properties between the corona and the underlying chromosphere and photosphere

are lumped into the boundary conditions. The last decade has seen a continuing debate about the precise form of these boundary conditions. The debate is mainly about whether line-tied or flow-through boundary conditions are the most appropriate ones. Line-tied boundary conditions correspond with rigid wall conditions, i.e., all velocity components vanish at the endpoints, whereas flow-through boundary conditions only prohibit motions perpendicular to the magnetic field. Recently, however, it has been recognized that both types of boundary conditions may be too severe and that modeling of the underlying atmosphere is important. See, for example, Van der Linden et al. (1994) who studied the influence of the stratification of the solar atmosphere on the stability of magnetic structures and who showed that near marginal stability both types of boundary conditions are violated. Mok & Van Hoven (1995) have performed interesting numerical calculations of the dynamical properties of a realistic thermal-structure interface between a coronal loop and the chromosphere/photosphere and qualitatively confirmed the discontinuous density and temperature model of Hollweg (1984).

The aim of this paper is to describe the influence of the chromospheric/photospheric layers on the continuous spectrum of coronal loops. This is of fundamental interest for wave heating theories of the solar corona. Inclusion of the chromospheric/photospheric layers automatically leads to two-dimensional equilibria. Of special interest is the coupling between Alfvén and slow magnetosonic continuum waves induced by this two-dimensionality. Poedts et al. (1985) and Poedts & Goossens (1991) were the first to study two-dimensional continua in coronal context. We derive the equations governing the continuous spectra for two-dimensional equilibria including gravity in general curvilinear coordinates. Next, this set of equations is solved numerically for coronal magnetic flux tubes with varying cross-sections and with the ends located in the high-beta, flux concentrated chromospheric/photospheric regions. This calculation requires an accurate, explicit, two-dimensional equilibrium of the expanding flux tube. Such equilibria are obtained by means of the numerical equilibrium program PARIS, introduced in a previous paper (Beliën et al. 1996b).

This paper is organized as follows. In Sect. 2, the model of a coronal magnetic flux tube is described. In Sect. 3, the equations for the continuous spectrum in such tubes are derived and the properties of these equations are discussed. In Sect. 4, we show some typical results. Finally, in Sect. 5 our conclusions are formulated. An appendix is devoted to the derivation of the equations for the continuous spectrum.

2. Flux tube model and equilibrium

As a model for a coronal loop, we consider a deformed cylindrical flux tube of length L and radius R , which is threaded by a magnetic field and embedded in a field-free medium. The curvature of the magnetic axis of the tube is neglected. A cylindrical coordinate system (r, θ, z) is adopted, with the z -axis along the axis of the tube. The flux tube is axisymmetric and, hence, none of the static equilibrium quantities depends on the

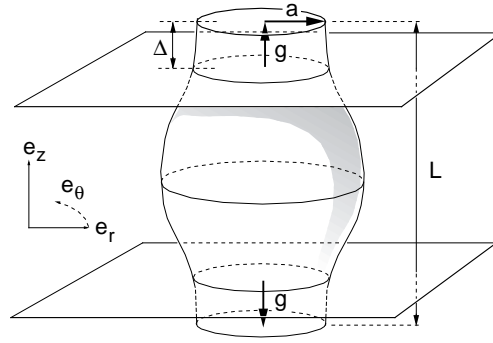


Fig. 1. Model of an expanded coronal magnetic flux tube.

azimuthal coordinate θ . The ends of the tube represent the chromosphere/photosphere while the mid-plane of the tube represents the apex of the loop. This model is described in Beliën et al. (1996b) and the geometry is illustrated in Fig. 1.

The cross-sections of flux tubes are in general not constant along the loop axis. For example, at the very base of coronal loops, i.e., in the convection layer, the magnetic flux is concentrated in several narrow tubes. As the magnetic field lines penetrate the photosphere and chromosphere they fan out due to a decrease of the confining pressure. In our model, in which we focus on single flux tubes, the variation of the cross-section is incorporated in the description of the z -dependence of the tube radius $r = R(z)$. We consider expanded tubes only, i.e., tubes having larger cross-sections at the top than at the bottom.

In the corona, the pressure scale height is of the order of 50 Mm (Priest 1982). Because the height of most flux tubes is much smaller, the influence of gravity can be neglected in the coronal part. However, in the chromospheric and photospheric parts of the flux tube, the scale height can be as small as a few hundred kilometers and the influence of gravity cannot be neglected. In our model, its effects are included by considering regions of length Δ near the bases of the flux tube in which the gravity is non-zero. In these regions, the gravitational field is aligned along the z -axis and it is directed towards the ends of the tube. In the coronal part of the flux tube gravity is neglected.

The magnetostatic equilibrium equations read:

$$\mathbf{J} \times \mathbf{B} = \nabla P - \rho \mathbf{g}, \quad \mu_0 \mathbf{J} = \nabla \times \mathbf{B}, \quad \nabla \cdot \mathbf{B} = 0, \quad (1)$$

where the magnetic field, the current density, the pressure, and the plasma density are denoted by \mathbf{B} , \mathbf{J} , P , and ρ , respectively. The magnetic field in axisymmetric cylindrical geometries may be written as:

$$\mathbf{B} = \nabla \psi \times \nabla \theta + f \nabla \theta, \quad (2)$$

where $2\pi\psi(r, z)$ is the magnetic flux through a circle with radius r at height z , and $f = f(\psi) \equiv rB_\theta$. The current density can then be written as

$$\mu_0 \mathbf{J} = -\Delta^* \psi \nabla \theta + \frac{df}{d\psi} \nabla \psi \times \nabla \theta, \quad (3)$$

where Δ^* is the Grad-Shafranov differential operator:

$$\Delta^* \equiv r^2 \nabla \cdot \frac{1}{r^2} \nabla. \quad (4)$$

From force balance it then follows that the basic equations may be written as (see Low 1975, and Beliën et al. 1996b):

$$P(\psi, z) = P_0(\psi) + \int_0^z \rho(\psi, z') g(z') dz', \quad (5)$$

$$\Delta^* \psi = -f \frac{df}{d\psi} - \mu_0 r^2 \frac{\partial P}{\partial \psi}, \quad (6)$$

where $P_0(\psi)$, $\rho(\psi)$, and $g(z)$ are free equilibrium profiles. Although the shape $r = R(z)$ of the flux tube is determined by pressure balance between the internal and external plasma, we here specify it a priori in order to avoid the complicated solution of a free boundary problem. Furthermore, boundary conditions at the ends of the flux tube ($z = 0$ and $z = L$) and at the outermost flux surface at $r = R(z)$ should be imposed.

We consider a class of equilibria for which the dependence of ρ on ψ and z is separable, i.e., $\rho(\psi, z) = \sigma(\psi)\tau(z)$. Furthermore, we consider equilibrium classes for which $P_0(\psi) = \sigma(\psi)$ so that $P(\psi, z)$ is separable also:

$$P(\psi, z) = \sigma(\psi)S(z), \quad S(z) \equiv 1 + \int_0^z \tau(z')g(z')dz'. \quad (7)$$

This choice of equilibria still contains an infinite amount of freedom through the profiles $f(\psi)$, $\sigma(\psi)$, $\tau(z)$, and $g(z)$. We distinguish the freedom in amplitudes from the freedom in profile form. Two profiles of order unity, viz., F and Π , are introduced such that

$$\frac{1}{2} \frac{df^2(\psi)}{d\psi} = AF(\psi), \quad \frac{d\sigma(\psi)}{d\psi} = -AB\Pi(\psi), \quad (8)$$

where A and B determine the amplitudes of $df^2/d\psi$ and $d\sigma/d\psi$. The equilibrium problem then transforms to the solution of the partial differential equation

$$\Delta^* \psi = A [-F(\psi) + Br^2 S(z)\Pi(\psi)]. \quad (9)$$

The other free equilibrium profiles, viz., $\tau(z)$, and $g(z)$ are chosen as follows:

$$\tau(z) = \tau_b \times \begin{cases} \exp(-z/H) & (0 \leq z \leq \Delta) \\ \phi(z) \exp(-\Delta/H) & (\Delta < z < L - \Delta) \\ \exp((z-L)/H) & (L - \Delta \leq z \leq L) \end{cases}, \quad (10)$$

and

$$g(z) = g_0 \times \begin{cases} -1 & (0 \leq z \leq \Delta) \\ 0 & (\Delta < z < L - \Delta) \\ 1 & (L - \Delta \leq z \leq L) \end{cases}, \quad g_0 = \frac{1}{\tau_b H}, \quad (11)$$

where H is the pressure scale height determined by the strength of gravity, τ_b is the normalization of the density. The profile $\phi(z)$

can be used to model an additional stratification of the density in the region where $g = 0$:

$$\phi(z) = \left[\mu + (1 - \mu) \left(\frac{z - L/2}{\Delta - L/2} \right)^{2\nu} \right]^{-1}, \quad (12)$$

where μ is the ratio between the density at $z = \Delta$ and $z = L/2$, and ν determines how fast the transition from $\tau(\Delta)$ to $\tau(L/2)$ takes place.

In the next section, the continuum equations are derived for a flux coordinate system. Therefore, all equilibrium quantities should be expressed in terms of the flux coordinates (ψ, θ, ζ) , where ζ is a longitudinal coordinate in the flux surfaces. Because Eq. (6) is initially solved on a structured (r_i, z_j) grid, this implies that a grid inversion needs to be carried out:

$$\begin{cases} \psi(r_i, z_j) \\ \zeta(r_i, z_j) \end{cases} \rightarrow \begin{cases} r(\psi_i, \zeta_j) \\ z(\psi_i, \zeta_j) \end{cases}. \quad (13)$$

Once this inversion has been carried out all physical quantities can be expressed in terms of the flux geometry and the free equilibrium profiles. For example, the contra- and covariant components of the magnetic field are given by:

$$\begin{aligned} B^1 &\equiv 0, & B^2 &= f(\psi)/r^2, & B^3 &= J^{-1}, \\ B_1 &= (g_{13}/g_{33})JB_p^2, & B_2 &= f(\psi), & B_3 &= JB_p^2, \end{aligned} \quad (14)$$

where the Jacobian $J = \partial(r, \theta, z)/\partial(\psi, \theta, \zeta)$ and $B_p = \sqrt{B_r^2 + B_z^2}$ is the poloidal magnetic field. For the solution of Eq. (6) we have used the numerical code PARIS described in Beliën et al. (1996b)). This code exploits isoparametric bicubic Hermite elements. It provides a very accurate grid inversion and a very accurate solution ψ for a moderate number of grid-points.

3. Two dimensional continuum equations

In terms of the fluid displacement field ξ , the linearized MHD equations can be cast in the following form:

$$\rho \frac{\partial^2 \xi}{\partial t^2} = \mathbf{B} \cdot \nabla \mathbf{b} + \mathbf{b} \cdot \nabla \mathbf{B} - \nabla \Pi + \hat{\rho} \mathbf{g}, \quad (15)$$

$$\mathbf{b} = \mathbf{B} \cdot \nabla \xi - \xi \cdot \nabla \mathbf{B} - \mathbf{B} \nabla \cdot \xi, \quad (16)$$

$$p = -\xi \cdot \nabla P - \gamma P \nabla \cdot \xi, \quad (17)$$

$$\hat{\rho} = -\xi \cdot \nabla \rho - \rho \nabla \cdot \xi, \quad (18)$$

$$\Pi \equiv p + \mathbf{B} \cdot \mathbf{b}, \quad (19)$$

where ρ , \mathbf{B} , and P are the equilibrium density, magnetic field, and pressure, respectively, and \mathbf{b} , p , $\hat{\rho}$, and Π are the perturbations of the magnetic field, pressure, density, and total pressure, respectively. This form of the linearized MHD equations shows that the derivatives of most of the perturbed quantities are in the direction parallel to the magnetic field (the $\mathbf{B} \cdot \nabla$ operators), whereas derivatives across the magnetic surfaces only occur through the terms $\nabla \cdot \xi$ and $\nabla \Pi$.

From Eqs. (2) and (3), it follows that $\mathbf{B} \cdot \nabla\psi = 0$ and $\mathbf{J} \cdot \nabla\psi = 0$. Hence, the magnetic field and current density lie on flux surfaces. Therefore, it is most natural to study the set of equations (15)–(19) in a flux coordinate system (ψ, θ, ζ) where θ and ζ are the coordinates used to describe positions within flux surfaces. We assume a time dependence $e^{-i\omega t}$, where ω is the angular frequency, and an azimuthal dependence $e^{im\theta}$, where m is the azimuthal mode number. Single azimuthal Fourier modes can be considered because the equilibrium is axisymmetric and, as a consequence, these Fourier modes do not couple. In terms of generalized flux coordinates ($q^1 = \psi$, $q^2 = \theta$, $q^3 = \zeta$), the linearized MHD equations can then be written in an elegant form that stresses derivatives across the magnetic flux surfaces (Kieras & Tataronis 1982, Poedts & Goossens 1991):

$$\frac{\partial \mathbf{X}}{\partial q^1} = \mathcal{A} \cdot \mathbf{X} + \mathcal{B} \cdot \mathbf{Y}, \quad (20)$$

$$\mathcal{C} \cdot \mathbf{Y} = \mathcal{D} \cdot \mathbf{X}, \quad (21)$$

$$b^1 = (\mathbf{B} \cdot \nabla) \xi^1, \quad (22)$$

where \mathbf{X} is a 2-vector and \mathbf{Y} is a 4-vector,

$$\mathbf{X} = [\xi^1, \Pi]^T, \quad \mathbf{Y} = [\xi^2, \xi^3, b^2, b^3]^T, \quad (23)$$

and \mathcal{A} , \mathcal{B} , \mathcal{C} , and \mathcal{D} are rectangular matrix operators. In the latter, ω and q^1 appear as *parameters* and the derivatives of q^2 and q^3 only appear as *linear* combinations of *first order* derivatives. Both ξ and \mathbf{b} are expressed in contravariant form, i.e., $\xi^i = \xi \cdot \nabla q^i$, and $b^i = \mathbf{b} \cdot \nabla q^i$. An explicit form of these equations is given in the appendix.

A formal way of solving Eqs. (20)–(22) is to invert Eq. (21), i.e.,

$$\mathbf{Y} = \mathcal{C}^{-1} \cdot \mathcal{D} \cdot \mathbf{X}, \quad (24)$$

and to substitute the result in Eq. (20) to obtain a partial differential equation for \mathbf{X} that may be solved subject to appropriate boundary conditions. This formal solution breaks down on flux surfaces $q^1 = q_0^1$ for which

$$\mathcal{C}(q_0^1, \omega^2) \cdot \mathbf{Y} = 0. \quad (25)$$

Eq. (25) supplemented with the appropriate longitudinal and azimuthal boundary conditions constitute a discrete eigenvalue problem on each flux surface q_0^1 . This equation determines the continuous spectrum. By varying q_0^1 , each discrete eigenvalue traces out a continuous set of eigenvalues $\{\omega\}$, i.e., a continuum branch. The totality of branches constitute the continuous spectrum. The flux surfaces q_0^1 on which the formal solution method breaks down are singular surfaces in the sense that the corresponding continuum ‘eigenfunctions’ are singular at q_0^1 (Goedbloed 1975).

The above equation can be reduced further to yield an explicit eigenvalue formulation. By elimination of b^2 and b^3 from Eq. (25), we obtain two coupled ordinary differential equations determining the continuous spectra, viz.,

$$(\mathcal{F} \mathbf{K} \mathcal{F} + \mathbf{H} + \mathbf{G}) \cdot \xi^t = \rho \omega^2 \mathbf{E} \cdot \xi^t, \quad (26)$$

where

$$\begin{aligned} \mathcal{F} &\equiv -iB^i \frac{\partial}{\partial q^i} = -iB^2 \frac{\partial}{\partial \theta} - iB^3 \frac{\partial}{\partial \zeta}, \\ \xi^t &= \begin{bmatrix} \xi^2(\zeta) \\ \xi^3(\zeta) \end{bmatrix} e^{im\theta - i\omega t}, \end{aligned} \quad (27)$$

and

$$\begin{aligned} \mathbf{E} &= \begin{bmatrix} g_{22} & 0 \\ 0 & g_{33} \end{bmatrix}, \\ \mathbf{K} &= \mathbf{E} - \frac{1}{\gamma P + |B|^2} \begin{bmatrix} B_2 B_2 & B_2 B_3 \\ B_3 B_2 & B_3 B_3 \end{bmatrix}, \quad |B|^2 = B_n B^n, \\ \mathbf{H} &= \mathbf{H}(\mathcal{F}, \gamma P, B_i, \frac{\partial B^i}{\partial \zeta}, \frac{\partial^2 B^i}{\partial \zeta^2}), \\ \mathbf{G} &= \mathbf{G}(\mathcal{F}, \gamma P, \rho g_3, B_i, \frac{\partial B^i}{\partial \zeta}). \end{aligned} \quad (28)$$

Explicit forms of \mathbf{G} and \mathbf{H} appear in the appendix: Eqs. (A21) and (A22). Gravity only appears in the matrix \mathbf{G} and $g_3 = g(z)(J/r)\partial\psi/\partial r$ is the third covariant component of the gravitational acceleration.

Since all matrices are Hermitian, Eq. (26) supplemented with the boundary conditions is a Hermitian eigenvalue problem. Hence, the eigenvalues ω^2 are all real. When $\omega^2 > 0$, the solutions represent stable oscillating continuum waves but when $\omega^2 < 0$, the solutions represent unstable continuum waves. The numerically calculated continua in this paper are all stable.

In Poedts & Goossens (1991), Eq. (26) was evaluated for an arcade model in a special geometry (constant Jacobian with the contravariant magnetic field components only depending on the flux coordinate) so that the \mathbf{H} matrix vanished. Furthermore, gravity was not taken into account so that the matrix \mathbf{G} vanished as well.

When B_2 is zero, i.e., when the magnetic field is untwisted, the two differential equations (26) are no longer coupled and split into separate equations for the well-known Alfvén and slow magnetosonic continua. The Alfvén wave solutions have $\xi^2 \neq 0$, $\xi^3 = 0$, which is the usual polarization perpendicular to the magnetic field. The slow magnetosonic wave solutions have $\xi^2 = 0$, $\xi^3 \neq 0$ and are polarized parallel to the magnetic field. From Eq. (26) and the explicit forms of the matrices \mathbf{H} and \mathbf{G} in the appendix, it can easily be seen that gravity does not influence the Alfvén continua in the case of untwisted magnetic fields. This is due to the fact that the polarization of the Alfvén waves is perpendicular to the direction of the gravitational acceleration. However, the slow magnetosonic continua are influenced by gravity since the polarization of the corresponding waves has a non-zero component in the direction of gravity.

When B_2 is non-zero, the components ξ^2 and ξ^3 no longer correspond to displacements in a flux surface that are perpendicular and parallel to the magnetic field. Although the notion of pure Alfvén and slow magnetosonic continuum waves must be abandoned when $B_2 \neq 0$, it is convenient to project Eq. (26) onto directions parallel and perpendicular to the magnetic field and to rewrite the equations in terms of the parallel and

perpendicular displacement components. The projected equations clearly show the coupling between Alfvén and slow magnetosonic continuum waves and are helpful in interpreting the results obtained in the next section. Within an astrophysical context these projected equations were first derived by Poedts et al. (1985). Within a plasma fusion context they were derived, without taking into account gravity effects, by Goedbloed (1975) and Pao (1975). To get a nice symmetrical form of the projected equations the following variables are used:

$$\begin{aligned}\tilde{\xi}_\perp &\equiv \frac{f}{rB_p|B|}\xi_\perp \approx \frac{B_2 B^3 \xi^2 - B^2 \xi^3}{B^3 |B|^2}, \\ \tilde{\xi}_\parallel &\equiv \frac{1}{|B|}\xi_\parallel \approx \frac{B_2 \xi^2 + B_3 \xi^3}{|B|^2}.\end{aligned}\quad (29)$$

The approximation signs indicate that the continuum ordering (Goedbloed 1975), i.e., $\partial \xi^1 / \partial \psi$ is of the same order as ξ^2 and ξ^3 but much larger than ξ^1 , has been used to eliminate ξ^1 from the definitions of $\tilde{\xi}_\parallel$ and $\tilde{\xi}_\perp$. Equality holds when the coordinate system is orthogonal. After some tedious algebra one then finds the following symmetric form of the continuum equations in terms of the components $\tilde{\xi}_\perp$ and $\tilde{\xi}_\parallel$:

$$(-\rho\omega^2 \mathbf{M} + \mathbf{N} + \mathbf{O} + \mathbf{G}) \cdot \tilde{\xi}^t = 0, \quad (30)$$

where

$$\tilde{\xi}^t = \begin{bmatrix} \tilde{\xi}_\perp(\zeta) \\ \tilde{\xi}_\parallel(\zeta) \end{bmatrix} e^{im\theta - i\omega t}, \quad (31)$$

and

$$\begin{aligned}\mathbf{M} &= \begin{bmatrix} \mathcal{M}|B|^2 & 0 \\ 0 & |B|^2 \end{bmatrix}, \\ \mathbf{N} &= \begin{bmatrix} |B|^2 \mathcal{F} \frac{\mathcal{M}}{|B|^2} \mathcal{F} |B|^2 + \mathcal{N} \left(\frac{1}{JB} \frac{\partial |B|^2}{\partial \zeta} \right)^2 & 0 \\ 0 & \mathcal{N} \mathcal{N} |B|^2 \mathcal{F} \end{bmatrix}, \\ \mathbf{O} &= \begin{bmatrix} 0 & \frac{i}{J} \frac{\partial |B|^2}{\partial \zeta} \mathcal{N} \mathcal{F} \\ -i \mathcal{F} \mathcal{N} \frac{1}{J} \frac{\partial |B|^2}{\partial \zeta} & 0 \end{bmatrix}, \\ \mathbf{G} &= \begin{bmatrix} -\frac{2}{J|B|^2} \frac{\partial |B|^2}{\partial \zeta} U & -iU|B|^2 \mathcal{F} \frac{1}{|B|^2} \\ \frac{i}{|B|^2} \mathcal{F} |B|^2 U & -\frac{1}{J} \frac{\partial U}{\partial \zeta} \end{bmatrix} + V \begin{bmatrix} 1 & -1 \\ -1 & 1 \end{bmatrix}.\end{aligned}\quad (32)$$

The variables \mathcal{M} , \mathcal{N} , U , and V are defined by:

$$\begin{aligned}\mathcal{M} &\equiv \frac{r^2 B_p^2}{f^2}, \\ \mathcal{N} &\equiv \frac{\gamma P}{\gamma P + |B|^2}, \\ U &\equiv \frac{|B|^2}{\gamma P + |B|^2} \rho \mathbf{g} \cdot \mathbf{B} = -\frac{|B|^2}{\gamma P + |B|^2} \frac{\rho}{J} \frac{\partial \Phi}{\partial \zeta} \\ V &\equiv \rho \mathbf{B} \cdot \left[\mathbf{g} \left(\frac{1}{\rho} \nabla \rho - \frac{1}{\gamma P + |B|^2} \rho \mathbf{g} \right) \right] \cdot \mathbf{B}, \\ &= -\frac{\rho}{J} \frac{\partial \Phi}{\partial \zeta} \left[\frac{1}{\rho J} \frac{\partial \rho}{\partial \zeta} + \frac{1}{\gamma P + |B|^2} \frac{\rho}{J} \frac{\partial \Phi}{\partial \zeta} \right],\end{aligned}\quad (33)$$

where we introduced the gravitational potential Φ ($\nabla \Phi = -\mathbf{g}$). The term between square brackets in the definition of V is a modification of the Brünt-Väisälä frequency which now becomes a *tensor*. The eigenvalue equation (30) formally corresponds to Eq. (57) of Poedts et al. (1985), but the explicit expressions involving the matrices \mathbf{M} , \mathbf{N} , \mathbf{O} , and \mathbf{G} have been simplified substantially here.

The matrices \mathbf{M} and \mathbf{N} are both diagonal representing the uncoupled Alfvén and slow magnetosonic continuum waves. The matrix \mathbf{O} is an off-diagonal matrix with non-zero elements when both \mathcal{N} and $\partial |B|^2 / \partial \zeta \neq 0$, i.e., the pressure and the geodesic curvature of the magnetic field should not vanish. Therefore, if one includes the chromospheric/photospheric boundary regions in a spectral study of coronal magnetic flux tubes, one can expect considerable coupling between Alfvén and slow magnetosonic waves. It should be noted that the coupling between these two types of continuum waves occurs if and only if the considered equilibrium is two-dimensional. For one-dimensional equilibria the geodesic curvature is zero and the component of the gravitational acceleration along the magnetic field necessarily vanishes.

3.1. Boundary conditions

Until now we have not specified what kind of boundary conditions we impose on the displacement vector field. By taking an azimuthal dependence of the form $\exp(im\theta)$ with integer m we have already implicitly assumed periodicity in the angle θ . The longitudinal boundary conditions need to be specified yet. The results shown in the next section are obtained with periodic longitudinal boundary conditions. Clearly, coronal magnetic flux tubes are not periodic structures. However, as a consequence of the huge density stratification, the amplitudes and derivatives at the bases are extremely small compared with the amplitudes and derivatives at the apex. Hence, we do not have to force the amplitude to be zero by means of the boundary conditions, i.e., we do not have to impose line-tied or flow-through boundary conditions, and we can just use periodic boundary conditions.

4. Numerical results

In this section, we present numerically obtained continuous spectra for coronal magnetic flux tubes with bases situated in high-beta chromospheric/photospheric plasma regions.

The equilibrium and the necessary metric tensor elements are determined with the equilibrium code PARIS. The spectral equations (26) or (30) are then solved on each flux surface by means of bicubic Hermite finite elements. Convergence studies have been made for each example to make sure that the results are reliable.

For all the examples shown in this section the boundary shape $R(z)$ is chosen as

$$R(z) = 1 + 16 (R_{\text{top}} - 1) (z/L)^2 (1 - z/L)^2, \quad (34)$$

where the parameter R_{top} determines the expansion of the loop at $z = L/2$ (the top of the flux tube). This form of the boundary

shape was chosen to illustrate the effect of expansion of the flux tube on the continuous spectrum. It is not meant to be a truly realistic flux tube shape. As mentioned in Sect. 2, we force the radial magnetic field component B_r to vanish at both ends of the flux tube. Hence, the magnetic field is purely vertical there. The shape (34) has been chosen accordingly to guarantee that $dR(z)/dz = 0$ at both ends. The equilibrium profiles F and Π are chosen as

$$F(\psi) = 6.75\psi(1 - \psi)^2, \quad \Pi(\psi) = 1 - \psi,$$

so that F is zero for $\psi = 0$ and $\psi = 1$ and it reaches its maximum of 1 at $\psi = 1/3$. The values of the equilibrium parameters of Eq. (8) are given by $A = 0.074$ and $B = 6.0$, respectively. The pressure at the boundary is given by $\sigma_1 = 1.75$. Unless stated otherwise, the aspect ratio $L/a = 20\pi$ and $R_{\text{top}} = 2.0$.

In the next subsection we examine the two-dimensional continua for a typical flux tube. Effects of expansion are considered in Sect. 4.2 and continua for a flux tube with an additional density stratification are studied in Sect. 4.3.

4.1. Example: an expanded flux tube

In this subsection we present and discuss the continuous spectra for a typical expanded flux tube. We choose the following values of the parameters: the pressure scale height $H = 0.05L$, the length of the gravitational region $\Delta = 0.25L$, and the density ratio $\mu = 1$. In Fig. 2a and b the longitudinal dependence of the equilibrium density, the total magnetic field, and the parameter $\beta \equiv 2P/|B|^2$ are shown. The former is plotted at the boundary flux surface ($\psi = 1$) while the latter two profiles are plotted on axis ($\psi = 0$). In Fig. 2c the magnetic twist Φ and the pressure function σ are plotted versus ψ . Here, the twist of magnetic field lines is defined by

$$\Phi = \int_0^L \frac{f}{r^2} J d\zeta. \quad (35)$$

The small increase of the plasma β in the top region is due to the fact that the pressure is constant in this region while the magnetic pressure is a monotonically decreasing function of z/L on the interval $[0, 0.5]$. The latter decrease is a consequence of the increase of the cross-section of the flux tube and flux conservation. Since β remains smaller than 0.1 this peculiarity does not influence the continuum frequencies very much.

In Fig. 3 the branches of the continuous spectrum are plotted as a function of $\sqrt{\psi}$ for the azimuthal mode number $m = -2$. A straight field line flux coordinate grid with 120 radial and 40 longitudinal grid points has been used to obtain good accuracy. With an orthogonal grid we found spurious unstable continuous spectra which were eliminated by using a straight field line grid. Only by using many more longitudinal grid points could we get rid of the instabilities introduced by the orthogonal flux grid. Also, the lowest frequency continuum branch showed some deviations with respect to the straight field line coordinate grid. However, for the higher frequencies branches the difference between results for the two grids becomes small.

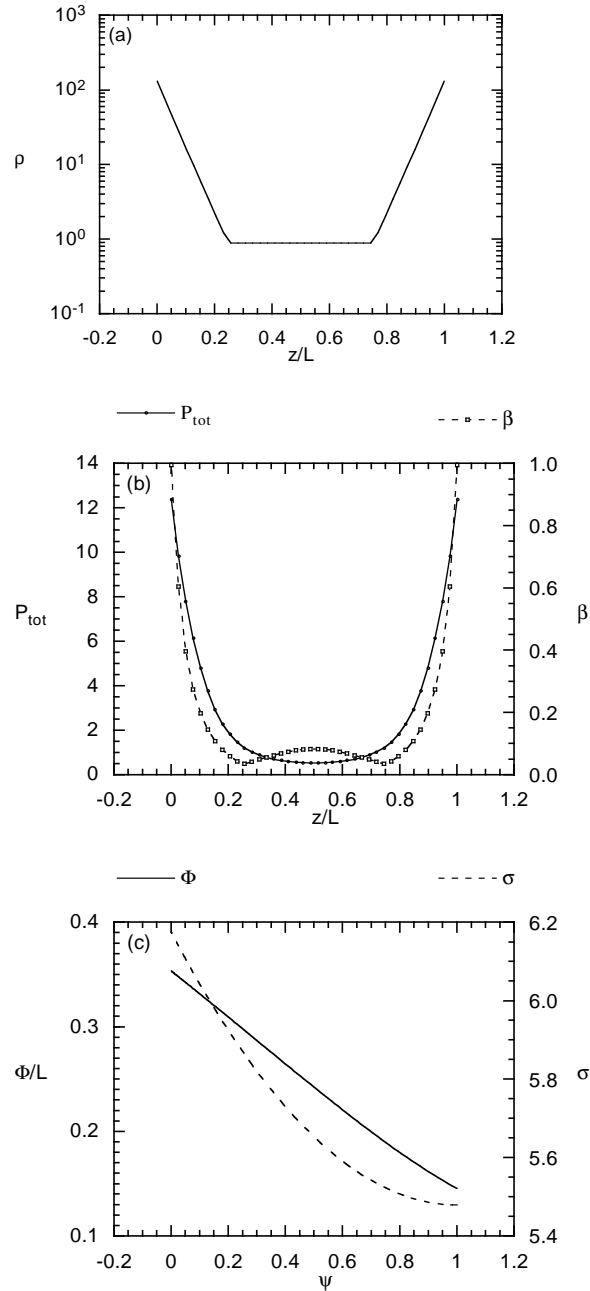


Fig. 2a–c. Equilibrium profiles: **a** Density on the $\psi = 1$ boundary surface. **b** Total pressure and plasma beta on axis. **c** Twist of the magnetic field and the pressure function σ versus ψ .

Two types of continuum branches can easily be distinguished in Fig. 3. The five strongly wiggling branches are Alfvén-like, whereas the other branches are slow-like. This distinction is based on the wave polarization, as will be discussed below. Coupling between the Alfvén-like branches, due to flux tube expansion and gravitational stratification, leads to avoided crossings and the formation of gaps. These gaps are larger for lower frequencies indicating that the lower frequency branches experience a stronger coupling. For the slow-like branches, this coupling is so strong that the branches become almost straight at

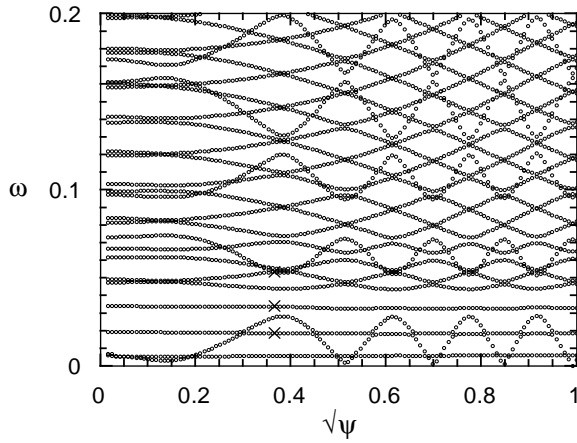


Fig. 3. Part of the $m = -2$ continuous spectrum belonging to the equilibrium configuration plotted in Fig. 2.

low frequencies. This behavior of the slow-like branches, which is observed in all our examples, is due to the gravitational stratification of the plasma density. For smaller stratification (larger values of H), the low frequency slow-like branches become similar to the higher frequency ones of Fig. 3. Coupling between Alfvén-like and slow-like branches is hardly visible. However, a very weak coupling is present between the ‘intersecting’ slow-like branch and lowest Alfvén-like branch at $\omega \approx 0.019$ and $\sqrt{\psi} \approx 0.57, 0.66, 0.74, 0.81, 0.88, 0.95$.

It is to be understood that the continuous spectrum is obtained by projecting all branches in Fig. 3 onto the ω -axis. By doing so it becomes clear that the entire ω -axis is covered by continuum frequencies, except for small regions around $\omega = 0.03$ and $\omega = 0.04$. These regions form gaps in the continuous spectrum. It was shown by Beliën et al. (1996a) that these gaps, which are truly due to the two-dimensionality of the considered equilibrium, facilitate the existence of *discrete global waves* with frequencies within the gaps. Since these waves are global, they should be easier to detect than continuum waves. Because the frequency of these waves depends on detailed equilibrium parameters, observation of these waves may provide a powerful diagnostic tool.

We now focus our attention on the proper part of the continuum waves. By ‘proper’ we mean the non-singular part of the eigenfunctions, i.e., the variation within the resonant flux surface rather than across the flux surface. In Fig. 4, we have plotted the ζ -dependence for three continuum waves that are all resonant (singular) on the $\sqrt{\psi} = 0.367$ flux surface. Note that we have plotted the parallel and perpendicular displacement components themselves instead of the components defined in Eq. (29).

Based on the amplitude ratios of the parallel and perpendicular components the waves are either called slow-like, when the parallel amplitude is larger, or Alfvén-like when the perpendicular amplitude is larger. Hence, the modes displayed in Fig. 4b and 4c are slow-like and the mode shown in Fig. 4a is Alfvén-like. The flux surface ($\sqrt{\psi} = 0.367$) is chosen rather

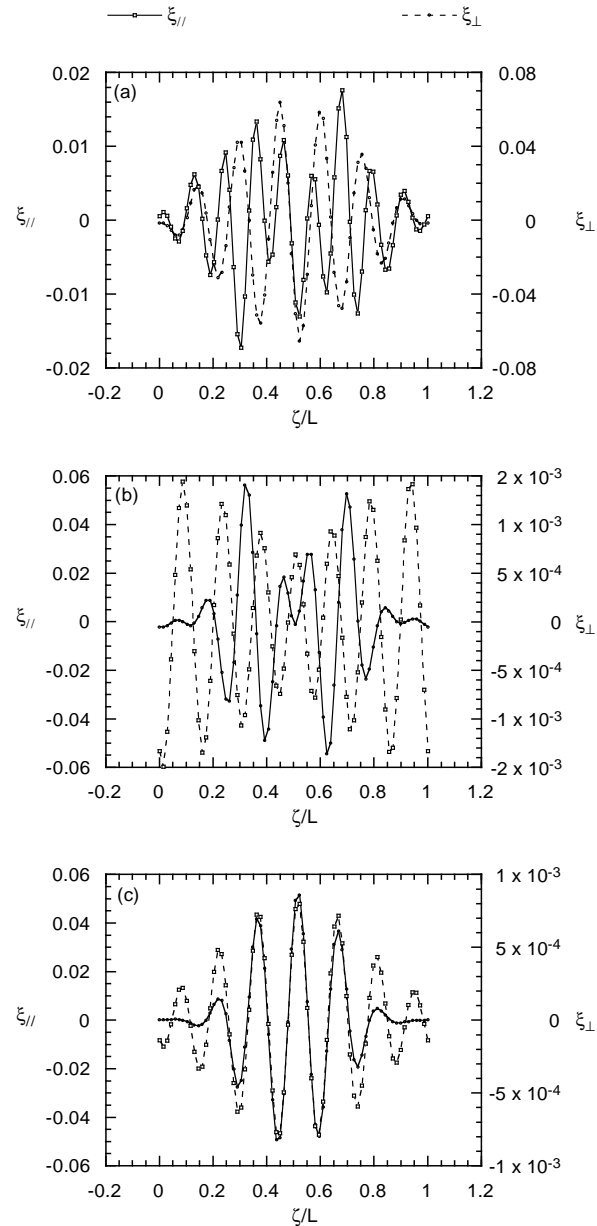


Fig. 4a–c. ζ -dependence of three continuum waves corresponding to the frequencies indicated by the crosses in Fig. 3: **a** $\omega = 0.0534$, **b** $\omega = 0.0340$, **c** $\omega = 0.0187$. In each frame the parallel as well as the perpendicular displacement components are shown.

arbitrarily, but the amplitude ratio of continuum waves on other flux surfaces corresponding to the same branches is very similar to that of Fig. 4. This is the basis of classifying the corresponding branches as either Alfvén-like or slow-like.

4.2. Effects of expansion

In this subsection we study the effects of expansion on the profile of the continuum branches and the polarization of the corresponding waves. The larger the expansion, i.e., the larger values of R_{top} in Eq. (34), the larger is the geodesic curvature

($\sim \partial|B|^2/\partial\zeta$) of the magnetic field lines. Hence, we can expect a larger coupling between Alfvén and slow magnetosonic continuum waves for larger flux tube expansions because of the coupling terms involving $\partial|B|^2/\partial\zeta$ of the matrix \mathbf{O} of Eq. (32). We consider two cases, one in which the flux tube is a straight cylinder (constant cross-section), and another one with a strong expansion ($R_{\text{top}} = 4$). We take the same equilibrium as used in the previous subsection. However, leaving the other equilibrium parameters unchanged would give β values above 0.15 at the top of the flux tube. To keep β at the top of the flux tube at the same value of Fig. 2, we have reset the scale height parameter H to $0.035L$. We have checked that this decrease of H only has a marginal influence on the continuous spectrum and the wave properties as compared to the case of the previous subsection ($H = 0.05L$).

In Fig. 5 some parts of the continuous spectra are shown for (a) $R_{\text{top}} = 4$ and (b) $R_{\text{top}} = 1$. Since the averaged magnetic field strength for $R_{\text{top}} = 1$ is smaller than for $R_{\text{top}} = 2$ and $R_{\text{top}} = 4$ and the order of magnitude of the continuum frequencies scales with the magnetic field strength, the $R_{\text{top}} = 1$ continuum branches have lower frequencies. We, therefore, plotted a smaller frequency range for $R_{\text{top}} = 1$. Qualitatively, the continuum branches have not changed much compared to the branches in Fig. 3. However, if we look at the polarization of the waves, in particular the Alfvén-like waves, we see that expansion of the flux tube has a large impact. Whereas for $R_{\text{top}} = 1.0$ the ratio $\xi_{\parallel}/\xi_{\perp}$ is less than 10^{-3} , it is of the order one for $R_{\text{top}} = 4$. From this we may conclude that the *polarization of coronal waves depends sensitively on the expansion of flux tubes*, whereas gravity has less effect. The implication for observations of MHD waves in the chromospheric/photospheric as well as the coronal regions is that one should determine both the parallel and the perpendicular velocity to establish the identity of the wave. This information could be obtained, for example, from non-thermal line broadening.

4.3. Additional non-gravitational density stratification

In this subsection, the continuous spectrum for a flux tube with an additional density stratification is discussed. Except for the density, the equilibrium configuration is the same as the one used for Fig. 3. The additional density stratification, displayed in Fig. 7, is obtained with the parameters $\mu = 0.01$ and $\nu = 1$ of Eq. (12). Such a stratification can model the transition region where the sharp temperature transition gives rise to an additional decrease in density.

Because the density is two orders of magnitude larger near the ends of the flux tube compared with the example displayed in Fig. 2, the averaged Alfvén velocity is smaller and, consequently, the continuum frequencies are lower. This can be seen in the Fig. 8b which shows a large density of continuum branches in a small frequency interval just above $\omega = 0$. Fig. 8 also reveals that the branches are flatter as compared to the continuum branches shown in Fig. 3 so that the continuous spectrum contains more gaps.

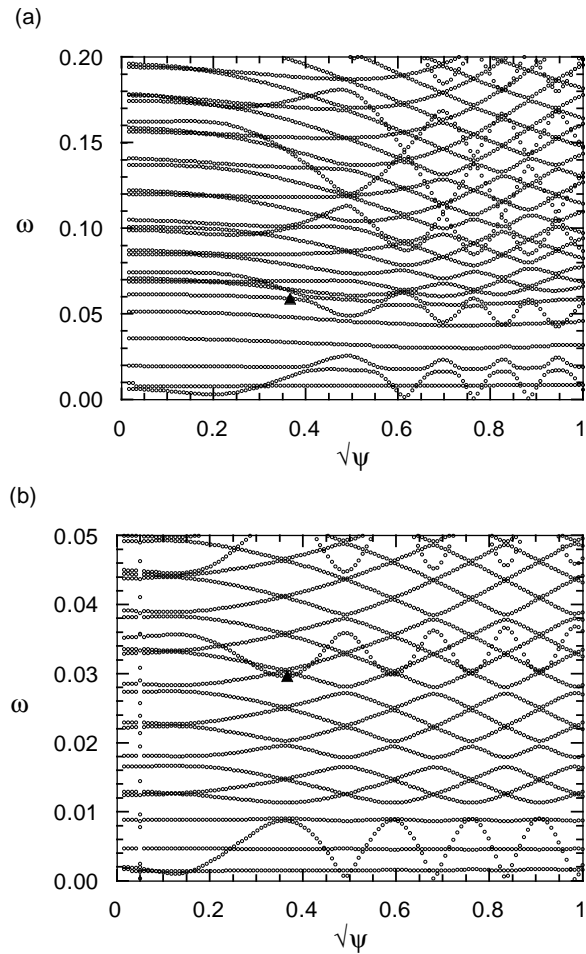


Fig. 5a and b. Parts of the $m = -2$ continuous spectra for **a** $R_{\text{top}} = 4$ and **b** $R_{\text{top}} = 1$. Equilibrium parameters are the same as those used to compute Fig. 3 except for H which has been set to $0.035L$ in the calculation of the continuous spectrum for $R_{\text{top}} = 4$.

The flattening of the continuum branches indicates that the continuous spectrum becomes less dependent on the twisting of the magnetic field so that it starts to resemble the behavior of line-tied continua. Recall that the continuous spectrum of a line-tied one-dimensional cylinder is proportional to $B_z(\psi)/\sqrt{\rho(\psi)}$, i.e., it is independent of the transverse magnetic field component (Halberstadt & Goedbloed 1994). For the present two-dimensional equilibria, this expression should be replaced by an average over the magnetic field lines. Since in our examples the average of $B_p/\sqrt{\rho}$ is a very weakly varying function of ψ , the flattening of the continuum branches is consistent with the continuous spectrum becoming more ‘line-tied’.

The additional density increase does not alter the coupling between Alfvén and slow magnetosonic waves qualitatively, as can be seen in Fig. 9. The amplitude ratios of the displacement components of the slow-like and Alfvén-like continuum waves are of the same order as in Fig. 4. From these results it follows that a density stratification contributes more to the coupling between similar continuum waves than between dissimilar ones.

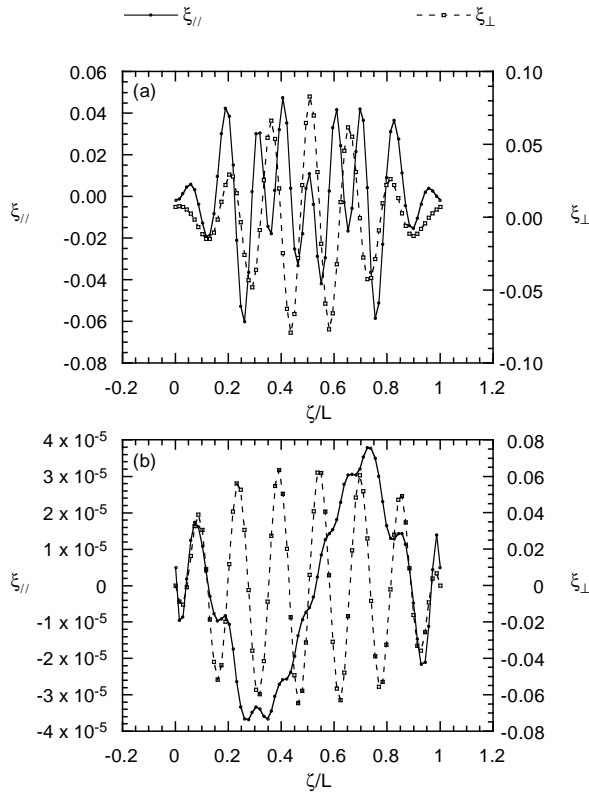


Fig. 6a and b. ζ -dependence of the two continuum waves with frequencies indicated by the triangles of Fig. 5: Alfvén-like continuum wave for **a** $R_{\text{top}} = 4$ and $\omega = 0.0589$, **b** Alfvén-like continuum wave for $R_{\text{top}} = 1$ and $\omega = 0.0296$.

5. Conclusions and perspective

In this paper, it has been shown that the properties of coronal continuum waves depend sensitively on the underlying dynamical structure of the chromospheric/photospheric boundary regions. The effect of these regions can be considered in several ways. In our model of coronal magnetic flux tubes, we have incorporated two effects of non-coronal origin that will have a direct effect on the Alfvén velocity and, therefore, on the MHD spectrum. These effects are:

1. magnetic flux concentration in the chromospheric/photospheric boundary regions,
2. density stratification due to gravity in the chromosphere and photosphere and a steep temperature rise in the transition zone.

The existence of continuous MHD spectra in inhomogeneous magnetic flux tubes is of fundamental importance for the heating of the solar corona by resonant absorption. Therefore, we studied the continuous spectra of magnetic flux tubes and paid special attention to the changes in the structure of the continuum branches and waves which are introduced by the above two effects.

The equations that determine the continuous spectrum have been written in a form that exploits the usual Alfvén and slow

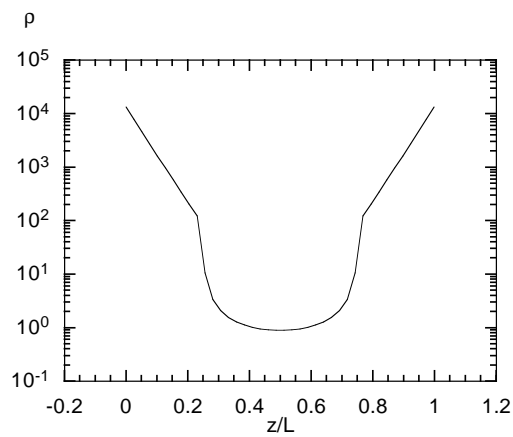


Fig. 7. The density as a function of z/L . Compared to Fig. 2 an additional non-gravitational density stratification is included.

magnetosonic polarization, i.e., the equations are written in terms of the parallel and perpendicular displacement components. These equations clearly reveal that gravity always couples Alfvén and slow magnetosonic continuum waves if the magnetic field is twisted. When the geodesic curvature of the magnetic field, i.e., the variation of the magnetic field strength within a magnetic surface, and the pressure are both non-zero Alfvén and slow magnetosonic continuum waves are also coupled. Therefore, pure Alfvén and slow magnetosonic continuum waves do not exist in coronal loops.

Our numerical results show that continuum branches can still be labeled Alfvén-like and slow-like on the basis of the amplitude ratio of the parallel and perpendicular displacement components. However, the Alfvén-like waves show much larger deviations from the pure ones than the slow-like waves. For Alfvén-like continuum waves the ratio $\xi_{\parallel}/\xi_{\perp}$ easily reaches values above 40% whereas for slow-like continuum waves the ratio $\xi_{\perp}/\xi_{\parallel}$ stays below 5%.

By varying the cross-section at the top of the flux tube we have found that the geodesic curvature has a more profound influence on the coupling between Alfvén- and slow-like continuum waves than the gravitational stratification. For example, the ratio $\xi_{\parallel}/\xi_{\perp}$ typically increases with a factor 10^3 for Alfvén-like waves going from a straight, constant cross-section, tube to one with a cross-section that is four times larger at the top than at the base.

Since the Alfvén-like continuum waves contain a substantial parallel component they are no longer incompressible. In nonlinear MHD, compressible motions are known to lead to the formation of shocks which can be dissipated easily. Therefore, the question arises how these waves evolve nonlinearly and what their role is for magnetic wave heating of the solar corona. We will report on this issue in a future publication.

Acknowledgements. This work was performed as part of the research programme of the ‘Stichting voor Fundamenteel Onderzoek der Materie’ (FOM) with financial support from the ‘Nederlandse Organisatie voor Wetenschappelijk Onderzoek’ (NWO) and the ‘Stichting

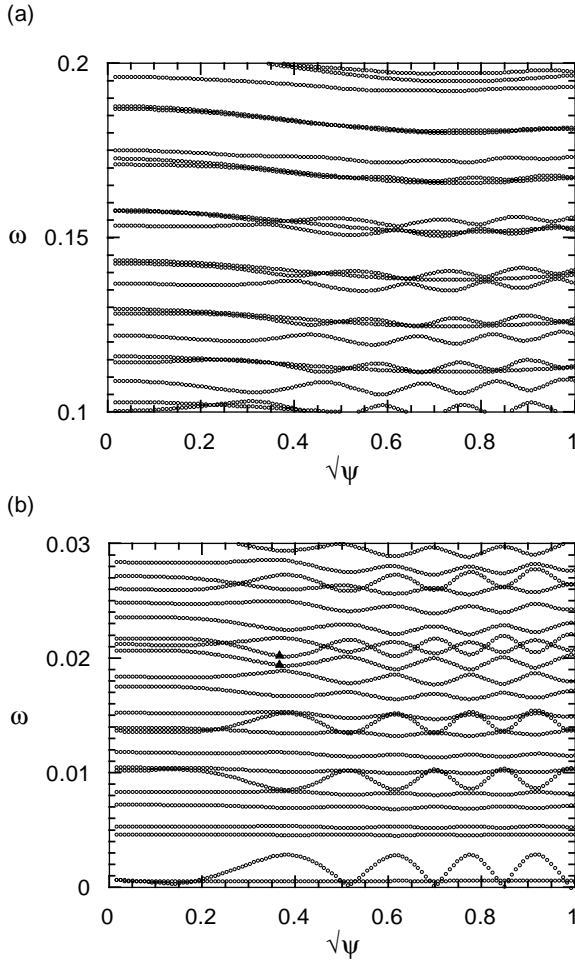


Fig. 8a and b. Parts of the $m = -2$ continuous spectrum belonging to the equilibrium configuration plotted in Fig. 7.

Academisch Rekencentrum Amsterdam' (SARA). Stimulating discussions with Hanno Holties, Ronald Nijboer, and Sasha Lifschitz are gratefully acknowledged.

Appendix A: derivation of the 2D continuum equations

In this appendix, we derive the equations governing the two-dimensional continua for axisymmetric magnetic flux tubes. The equations are derived for curvilinear coordinates. Hence, extensive use of tensor calculus is made (Arfken, 1990).

A flux coordinate system (q^1, q^2, q^3) is used in which the coordinate q^1 labels the flux surfaces. Since q^1 is a flux coordinate, $\mathbf{B} \cdot \nabla q^1 = 0$ and, hence, $B^1 = 0$. The covariant components of the metric tensor are denoted as g_{ij} . The Jacobian of the coordinate transformation is denoted by J . A g_n with a single subscript is a covariant component of the gravitational acceleration \mathbf{g} . The symbol \mathcal{F} represents the parallel gradient operator $-i\mathbf{B} \cdot \nabla$,

$$\mathcal{F} \equiv -iB^n \frac{\partial}{\partial q^n}. \quad (\text{A1})$$

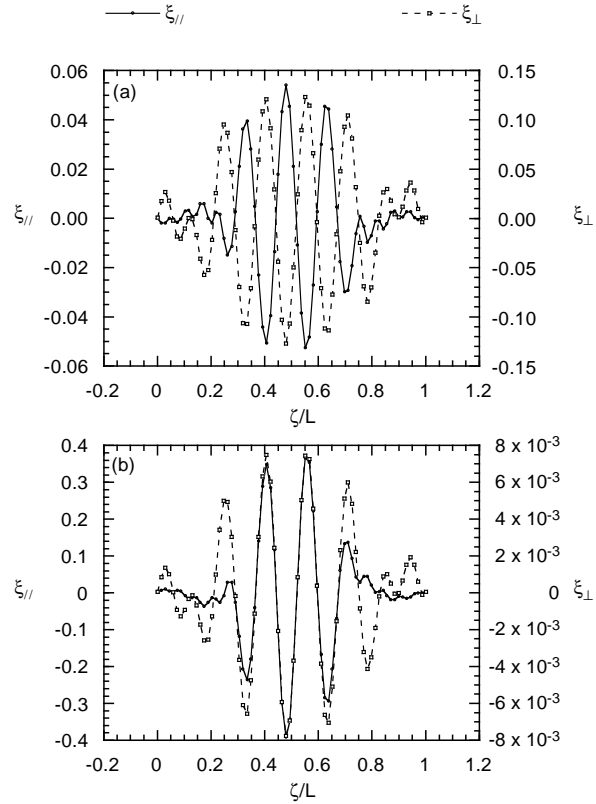


Fig. 9a and b. ζ -dependence of two continuum waves corresponding to the frequencies indicated by triangles in Fig. 8: **a** Alfvén-like continuum wave for $\omega = 0.0203$, **b** slow-like continuum wave for $\omega = 0.0195$.

A differential operator will work on all the factors to its right unless these factors are surrounded by parentheses in which case the differential operator only works on the factors between the parentheses. A last point of notation is the use of the Einstein convention for repeated indices.

The contravariant components of the perturbed magnetic field \mathbf{b} defined in Eq. (16) are given by:

$$b^1 = i\mathcal{F}\xi^1, \quad (\text{A2})$$

$$b^2 = -\frac{B^2}{J} \frac{\partial}{\partial q^k} (J\xi^k) - \xi^k \frac{\partial B^2}{\partial q^k} + i\mathcal{F}\xi^2, \quad (\text{A3})$$

$$b^3 = -\frac{B^3}{J} \frac{\partial}{\partial q^k} (J\xi^k) - \xi^k \frac{\partial B^3}{\partial q^k} + i\mathcal{F}\xi^3, \quad (\text{A4})$$

whereas Eqs. (17)–(18) for the perturbed pressure and the density become:

$$p = -\gamma P \frac{1}{J} \frac{\partial}{\partial q^k} (J\xi^k) - \xi^k \frac{\partial P}{\partial q^k}, \quad (\text{A5})$$

$$\hat{\rho} = -\frac{1}{J} \frac{\partial}{\partial q^k} (J\xi^k) \rho - \xi^k \frac{\partial \rho}{\partial q^k}. \quad (\text{A6})$$

Using Eqs. (A2)–(A5) and the equilibrium force balance equation, we can obtain an expression for $\nabla \cdot \xi$ in terms of the total

perturbed pressure Π and the contravariant displacement components, viz.,

$$\nabla \cdot \xi = \frac{1}{J} \frac{\partial}{\partial q^k} (J \xi^k) = \frac{1}{\gamma P + B_n B^n} \times \left\{ \left[i B_{k.} \mathcal{F} - B^3 \frac{\partial B_k}{\partial q^3} + B^i B^j \frac{\partial g_{ij}}{\partial q^k} - \rho g_k \right] \xi^k - \Pi \right\}. \quad (\text{A7})$$

From this equation it then follows that

$$\begin{aligned} \frac{\partial \xi^1}{\partial q^1} = & \left[-\frac{1}{J} \frac{\partial J}{\partial q^1} + \frac{1}{\gamma P + B_n B^n} \times \right. \\ & \left. \left(i B_{1.} \mathcal{F} - B^3 \frac{\partial B_1}{\partial q^3} + B^i B^j \frac{\partial g_{ij}}{\partial q^1} - \rho g_1 \right) \right] \xi^1 \\ & - \frac{1}{\gamma P + B_n B^n} \Pi + \left[\frac{1}{\gamma P + B_n B^n} i B_{2.} \mathcal{F} - \frac{\partial}{\partial q^2} \right] \xi^2 \\ & + \left[-\frac{1}{J} \frac{\partial J}{\partial q^3} - \frac{\partial}{\partial q^3} + \frac{1}{\gamma P + B_n B^n} \times \right. \\ & \left. \left(i B_{3.} \mathcal{F} - B^3 \frac{\partial B_3}{\partial q^3} + B^i B^j \frac{\partial g_{ij}}{\partial q^3} - \rho g_3 \right) \right] \xi^3. \quad (\text{A8}) \end{aligned}$$

On substitution of Eqs. (A7)–(A8) in the q^1 -component of the momentum equation (15), we obtain an expression for $\partial \Pi / \partial q^1$:

$$\begin{aligned} \frac{\partial \Pi}{\partial q^1} = & \left[\rho \omega^2 g_{11} - \mathcal{F} g_{11.} \mathcal{F} + i \left(\frac{\partial B_1}{\partial q^1} - B^i \frac{\partial g_{1i}}{\partial q^1} \right) \mathcal{F} \right. \\ & - \frac{\rho g_1}{\gamma P + B_n B^n} \left(i B_{1.} \mathcal{F} - B^3 \frac{\partial B_1}{\partial q^3} + B^i B^j \frac{\partial g_{ij}}{\partial q^1} - \rho g_1 \right) \\ & - \frac{\partial \rho}{\partial q^1} g_1 \left. \right] \xi^1 + \frac{\rho g_1}{\gamma P + B_n B^n} \Pi - \frac{\rho g_1}{\gamma P + B_n B^n} i B_{2.} \mathcal{F} \xi^2 \\ & - B^2 \frac{\partial g_{22}}{\partial q^1} b^2 + \left[i \mathcal{F} g_{13} + \frac{\partial B_1}{\partial q^3} - B^3 \frac{\partial g_{33}}{\partial q^1} \right] b^3 \\ & + \left[\rho \omega^2 g_{13} - \frac{\rho g_1}{\gamma P + B_n B^n} \left(i B_{3.} \mathcal{F} - B^3 \frac{\partial B_3}{\partial q^3} \right. \right. \\ & \left. \left. + B^i B^j \frac{\partial g_{ij}}{\partial q^3} - \rho g_3 \right) - \frac{\partial \rho}{\partial q^3} g_1 \right] \xi^3. \quad (\text{A9}) \end{aligned}$$

After substitution of Eq. (A7), the covariant form of the q^2 - and q^3 -components of the momentum equation (15) read:

$$\frac{\partial \Pi}{\partial q^2} - i \frac{\partial B_2}{\partial q^1} \mathcal{F} \xi^1 = \rho \omega^2 g_{22} \xi^2 + i \mathcal{F} g_{22} b^2, \quad (\text{A10})$$

and

$$\begin{aligned} \frac{\partial \Pi}{\partial q^3} - & \left[\rho \omega^2 g_{31} - \mathcal{F} g_{31.} \mathcal{F} + i \left(\frac{\partial B_3}{\partial q^1} - B^3 \frac{\partial g_{13}}{\partial q^3} \right) \mathcal{F} \right. \\ & - \frac{\rho g_3}{\gamma P + B_n B^n} \left(i B_{1.} \mathcal{F} - B^3 \frac{\partial B_1}{\partial q^3} + B^i B^j \frac{\partial g_{ij}}{\partial q^1} - \rho g_1 \right) \end{aligned}$$

$$\begin{aligned} - \frac{\partial \rho}{\partial q^1} g_3 \left. \right] \xi^1 = & -i \frac{\rho g_3}{\gamma P + B_n B^n} B_{2.} \mathcal{F} \xi^2 \\ & + \left[\rho \omega^2 g_{33} - \frac{\rho g_3}{\gamma P + B_n B^n} \left(i B_{3.} \mathcal{F} - B^3 \frac{\partial B_3}{\partial q^3} \right. \right. \\ & \left. \left. + B^i B^j \frac{\partial g_{ij}}{\partial q^3} - \rho g_3 \right) - \frac{\partial \rho}{\partial q^3} g_3 \right] \xi^3 \\ & - B^2 \frac{\partial g_{22}}{\partial q^3} b^2 + \left[i \mathcal{F} g_{33} + \frac{\partial B_3}{\partial q^3} - B^3 \frac{\partial g_{33}}{\partial q^3} \right] b^3. \quad (\text{A11}) \end{aligned}$$

In the same way, substitution of Eq. (A7) in Eq. (16) results in the following expressions for the q^2 - and q^3 -components of Eq. (16):

$$\begin{aligned} \left[\frac{\partial B^2}{\partial q^1} - \frac{B^2}{\gamma P + B_n B^n} \left(i B_{1.} \mathcal{F} - B^3 \frac{\partial B_1}{\partial q^3} \right. \right. \\ \left. \left. + B^i B^j \frac{\partial g_{ij}}{\partial q^1} - \rho g_1 \right) \right] \xi^1 - \frac{B^2}{\gamma P + B_n B^n} \Pi = \\ i \left(1 - \frac{B_2 B^2}{\gamma P + B_n B^n} \right) \mathcal{F} \xi^2 + \left[-\frac{\partial B^2}{\partial q^3} - \frac{B^2}{\gamma P + B_n B^n} \times \right. \\ \left. \left(i B_{3.} \mathcal{F} - B^3 \frac{\partial B_3}{\partial q^3} + B^i B^j \frac{\partial g_{ij}}{\partial q^3} - \rho g_3 \right) \right] \xi^3 - b^2, \quad (\text{A12}) \end{aligned}$$

and

$$\begin{aligned} \left[\frac{\partial B^3}{\partial q^1} - \frac{B^3}{\gamma P + B_n B^n} \left(i B_{1.} \mathcal{F} - B^3 \frac{\partial B_1}{\partial q^3} \right. \right. \\ \left. \left. + B^i B^j \frac{\partial g_{ij}}{\partial q^1} - \rho g_1 \right) \right] \xi^1 - \frac{B^3}{\gamma P + B_n B^n} \Pi = \\ -i \frac{B_2 B^3}{\gamma P + B_n B^n} \mathcal{F} \xi^2 + \left[i \left(1 - \frac{B_3 B^3}{\gamma P + B_n B^n} \right) \mathcal{F} \right. \\ \left. - \frac{\partial B^3}{\partial q^3} + \frac{B^3}{\gamma P + B_n B^n} \left(B^3 \frac{\partial B_3}{\partial q^3} - B^i B^j \frac{\partial g_{ij}}{\partial q^3} + \rho g_3 \right) \right] \xi^3 \\ - b^3. \quad (\text{A13}) \end{aligned}$$

The six equations (A8)–(A13) now have the required form expressed by Eqs. (20)–(21), where Eqs. (A8)–(A9) correspond to Eq. (20) while Eqs. (A10)–(A13) correspond to Eq. (21). The equations governing the continuum are found by equating the right hand sides of Eqs. (A10)–(A13) to zero:

$$\rho \omega^2 g_{22} \xi^2 + i \mathcal{F} g_{22} b^2 = 0, \quad (\text{A14})$$

$$\begin{aligned} -i \frac{\rho g_3}{\gamma P + B_n B^n} B_{2.} \mathcal{F} \xi^2 + \left[\rho \omega^2 g_{33} - \frac{\rho g_3}{\gamma P + B_n B^n} \times \right. \\ \left. \left(i B_{3.} \mathcal{F} - B^3 \frac{\partial B_3}{\partial q^3} + B^i B^j \frac{\partial g_{ij}}{\partial q^3} - \rho g_3 \right) \right] \xi^3 \\ - B^2 \frac{\partial g_{22}}{\partial q^3} b^2 + \left[i \mathcal{F} g_{33} + \frac{\partial B_3}{\partial q^3} - B^3 \frac{\partial g_{33}}{\partial q^3} \right] b^3 = 0, \quad (\text{A15}) \end{aligned}$$

$$i \left(1 - \frac{B_2 B^2}{\gamma P + B_n B^n} \right) \mathcal{F} \xi^2 + \left[-\frac{\partial B^2}{\partial q^3} - \frac{B^2}{\gamma P + B_n B^n} \times \left(i B_3 \mathcal{F} - B^3 \frac{\partial B_3}{\partial q^3} + B^i B^j \frac{\partial g_{ij}}{\partial q^3} - \rho g_3 \right) \right] \xi^3 - b^2 = 0, \quad (\text{A16})$$

$$-i \frac{B_2 B^3}{\gamma P + B_n B^n} \mathcal{F} \xi^2 + \left[i \left(1 - \frac{B_3 B^3}{\gamma P + B_n B^n} \right) \mathcal{F} - \frac{\partial B^3}{\partial q^3} + \frac{B^3}{\gamma P + B_n B^n} \left(B^3 \frac{\partial B_3}{\partial q^3} - B^i B^j \frac{\partial g_{ij}}{\partial q^3} + \rho g_3 \right) \right] \xi^3 - b^3 = 0. \quad (\text{A17})$$

Solving for b^2 and b^3 from Eqs. (A16)–(A17) and substituting the results in Eqs. (A14)–(A15) leads to the following set of coupled, ordinary second order differential equations in q^3 :

$$\rho \omega^2 \mathbf{E} \cdot \boldsymbol{\xi}^t = (\mathcal{F} \mathbf{K} \mathcal{F} + \mathbf{H} + \mathbf{G}) \cdot \boldsymbol{\xi}^t, \quad (\text{A18})$$

where

$$\boldsymbol{\xi}^t = \begin{bmatrix} \xi^2 \\ \xi^3 \end{bmatrix}, \quad (\text{A19})$$

$$\mathbf{E} = \begin{bmatrix} g_{22} & 0 \\ 0 & g_{33} \end{bmatrix},$$

$$\mathbf{K} = \mathbf{E} - \frac{1}{\gamma P + B_n B^n} \begin{bmatrix} B_2 B_2 & B_2 B_3 \\ B_3 B_2 & B_3 B_3 \end{bmatrix},$$

$$\mathbf{H} = \begin{bmatrix} H_{11} & H_{12} \\ H_{21} & H_{22} \end{bmatrix},$$

$$\mathbf{G} = \begin{bmatrix} G_{11} & G_{12} \\ G_{21} & G_{22} \end{bmatrix}. \quad (\text{A20})$$

The elements of the matrices \mathbf{H} and \mathbf{G} are given by:

$$\begin{aligned} H_{11} &= 0, \\ H_{12} &= i \mathcal{F} g_{22} \frac{\partial B^2}{\partial q^3} - i \mathcal{F} \frac{B_2}{\gamma P + B_k B^k} B_n \frac{\partial B^n}{\partial q^3}, \\ H_{21} &= -i g_{22} \frac{\partial B^2}{\partial q^3} \mathcal{F} + i \frac{B_2}{\gamma P + B_k B^k} B_n \frac{\partial B^n}{\partial q^3} \mathcal{F}, \\ H_{22} &= B^3 \frac{\partial}{\partial q^3} \left(\frac{\gamma P}{\gamma P + B_k B^k} g_{33} \frac{\partial B^3}{\partial q^3} \right) + \frac{\partial B^n}{\partial q^3} \frac{\partial B^m}{\partial q^3} \times \left(g_{nm} - \frac{B_n B_m}{\gamma P + B_k B^k} \right), \end{aligned} \quad (\text{A21})$$

and

$$\begin{aligned} G_{11} &= 0, \\ G_{12} &= -i \mathcal{F} \frac{B_2}{\gamma P + B_n B^n} \rho g_3, \\ G_{21} &= i \frac{B_2}{\gamma P + B_n B^n} \rho g_3 \mathcal{F}, \\ G_{22} &= -B^3 \frac{\partial}{\partial q^3} \left(\frac{B_3}{\gamma P + B_n B^n} \rho g_3 \right) - \frac{\rho g_3}{\gamma P + B_m B^m} \times \left(2 B_n \frac{\partial B^n}{\partial q^3} + \rho g_3 \right) + \frac{\partial \rho}{\partial q^3} g_3. \end{aligned} \quad (\text{A22})$$

In the derivation of Eqs. (A8)–(A22) we made use of the facts that the equilibrium quantities do not depend on q^2 , that B_2 is a flux function, and hence only depends on q^1 , and that $g_2 = 0$.

References

- Arfken, G. 1990, *Mathematical Methods for Physicists*, Academic Press, San Diego, CA
- Beliën, A.J.C., Poedts, S., Goedbloed, J.P. 1996a, *Phys. Rev. Lett.*, 76, 567
- Beliën, A.J.C., Poedts, S., Goedbloed, J.P. 1996b, submitted to *Comp. Phys. Comm.*
- Bocchialini, K., Baudin, F. 1995, *Astron. Astrophys.*, 299, 893
- Chen, L., Hasewaga, A. 1974, *J. Geophys. Res.*, 79, 1024
- Davila, J.M. 1987, *Astrophys. J.*, 317, 514
- Goedbloed, J.P. 1975, *Phys. Fluids*, 18, 1258
- Goedbloed, J.P., Halberstadt, G. 1994, *Astron. Astrophys.*, 286, 275
- Grossmann, W., Smith, R.A. 1988, *Astrophys. J.*, 332, 476
- Halberstadt, G., Goedbloed, J.P. 1993, *Astron. Astrophys.*, 280, 647
- Halberstadt, G., Goedbloed, J.P. 1995a, *Astron. Astrophys.*, 301, 559
- Halberstadt, G., Goedbloed, J.P. 1995b, *Astron. Astrophys.*, 301, 577
- Hameiri, E. 1981, *Phys. Fluids*, 24, 562
- Heyvaerts, J., Priest, E.R. 1983, *Astron. Astrophys.*, 117, 220
- Hollweg, J.V. 1984, *Astrophys. J.*, 272, 392
- Inson, J.A. 1978, *Astrophys. J.*, 226, 65
- Kieras, C.E., Tataronis, J.A. 1982, *J. Plasma Phys.*, 28, 395
- Krylov, A.L., Lifschitz, A.E., Fedorov, E.N. 1979, *Doklady Akademii Nauk SSSR*, 247, 1094
- Krylov, A.L., Lifschitz, A.E. 1984, *Planetary and Space Science*, 32, 481
- Kuperus, M., Inson, J.A., Spicer, D.S. 1981, *Ann. Rev. Astron. Astrophys.*, 19, 7
- Low, B.C. 1975, *Astrophys. J.*, 197, 251
- Mok, Y., van Hoven, G. 1995, *Solar Phys.*, 161, 67
- Mond, M., Hameiri, E., Hu, P.N. 1990, *J. Geophys. Res.*, 95(A1), 89
- Ofman, L., Davila, J.M. 1996, *Astrophys. Lett.*, 456, L123
- Ofman, L., Davila, J.M., Steinolfson, R.S. 1995, *Astrophys. J.*, 444, 471
- Pao, Y.P. 1975, *Nucl. Fusion*, 15, 631
- Poedts, S., Boynton, G.C. 1996, *Astron. Astrophys.*, 306, 610
- Poedts, S., Goossens, M. 1991, *Solar Phys.*, 133, 281
- Poedts, S., Hermans, D., Goossens, M. 1985, *Astron. Astrophys.*, 151, 16
- Poedts, S., Kerner, W. 1992, *J. Plasma Phys.*, 47, 139
- Poedts, S., Kerner, W., Goossens, M. 1989, *J. Plasma Phys.*, 42, 27
- Priest, E. 1982, *Solar Magnetohydrodynamics*, D. Reidel Publishing Company, Dordrecht, Holland
- Southwood, D.J., Kivelson, M.G. 1986, *J. Geophys. Res.*, 91, 6871
- Tataronis, J.A., Grossmann, W. 1973, *Z. Physik*, 261, 203
- van der Linden, R.A.M., Hood, A.W., Goedbloed, J.P. 1994, *Solar Phys.*, 154, 69
- Zirker, J.B. 1993, *Solar Phys.*, 148, 43